Volume 6
Number 1
January 2026
Pages 1–120

Environmental Science
Atmospheres

rsc.li/esatmospheres

ISSN 2634-3606

ROYAL SOCIETY OF CHEMISTRY

PAPER
Alexander Laskin *et al.*
Chemical imaging of individual stratospheric particles sampled over North America

Environmental Science: Atmospheres

ROYAL SOCIETY OF CHEMISTRY

PAPER

View Article Online
View Journal | View Issue

Cite this: *Environ. Sci.: Atmos.*, 2026, **6**, 47

Chemical imaging of individual stratospheric particles sampled over North America

Steven Sharpe, †[a] Yaowei Li, †[b] Sophia Benjemia,[a] Felipe Rivera-Adorno,[a] Temitope Olayemi,[a] Julius Ese,[a] Xiaoli Shen,[c] Matthew Fraund,[d] Ryan Moffet,[e] Nurun Nahar Lata,[f] Zezhen Cheng,[f] Swarup China,[f] Cameron R. Homeyer,[g] John Dykema,[b] Matthew A. Marcus,[h] Jian Wang,[i] Daniel Cziczo,[c] Frank Keutsch[b] and Alexander Laskin *[ac]

The increasing size, severity, and frequency of wildfires have led to dramatic increases in particulate matter concentrations in the troposphere. Severe wildfires can generate intense convective systems capable of transporting large quantities of biomass burning organic aerosols (BBOA) to the upper troposphere and lower stratosphere (UTLS). Chemically complex organic matter and light-absorbing carbonaceous material is introduced into stratospheric regions that were historically isolated from direct surface emissions. In this study, stratospheric particles were sampled over North America during the Dynamics and Chemistry of the Summer Stratosphere (DCOTSS) campaign, an aircraft-based research project designed to characterize convective perturbation in the UTLS. Particle samples collected from six research flights during summer 2022 were analyzed using Computer-Controlled Scanning Electron Microscopy and Scanning Transmission X-ray Microscopy to investigate particle size distributions, morphology, chemical composition, and mixing state of stratospheric particles along transects across the continental United States and adjacent Pacific Ocean airspace. Analysis revealed that all sampled particles contained detectable levels of carbon, with most exhibiting organic volume fractions of 0.37 ± 0.20. Notably, about 5% of the particles also contained soot inclusions, which indicates the presence of refractory black carbon transported to stratospheric altitudes and provides direct evidence of wildfire-derived black carbon reaching the UTLS. Typical particle morphology exhibits organic shells over soot and inorganic cores and suggests secondary processing and aging of BBOA during transport to and within the UTLS. These findings provide compelling evidence that wildfire emissions play a critical role in affecting the long-term composition and radiative properties of stratospheric particles.

Received 29th September 2025
Accepted 27th October 2025

DOI: 10.1039/d5ea00127g

rsc.li/esatmospheres

Environmental significance

This study demonstrates that wildfire emissions are responsible for a persistent shift in the composition of aerosols in the upper troposphere and lower stratosphere. Biomass burning organic aerosol transported by wildfire-driven convective systems contributes significantly to the organic enrichment of the stratospheric aerosol layer. These injections alter the chemical and physical properties of stratospheric particles, influencing their mixing state, morphology, and optical characteristics. As a result, wildfire smoke has the potential to significantly impact stratospheric radiative forcing and long-term atmospheric composition.

Introduction

Stratospheric aerosols are generally more chemically homogenous and longer-lived than the more complicated aerosols found in the troposphere.[1] Stratospheric aerosol is commonly categorized into three primary particle types: binary mixtures of sulfuric acid and water, sulfuric acid containing meteoritic metals, and occasional organic-sulfate particles originating

[a]*Department of Chemistry, Purdue University, West Lafayette, IN 47907, USA. E-mail: alaskin@purdue.edu*
[b]*School of Engineering and Applied Sciences, Harvard University, Cambridge, MA 02138, USA*
[c]*Department of Earth, Atmospheric, & Planetary Sciences, Purdue University, West Lafayette, IN 47907, USA*
[d]*Fraund Consulting, Pleasant Hill, California, CA 94523, USA*
[e]*Sonoma Technology, Inc., Petaluma, CA 94954, USA*
[f]*Enviomental Molecular Sciences Laboratory, Pacific Northwest National Laboratory, Richland, WA 99352, USA*
[g]*School of Meteorology, The University of Oklahoma, Norman, OK 73072, USA*
[h]*Advanced Light Source, Lawrence Berkeley National Laboratory, Berkely, CA 94720, USA*
[i]*Canadian Light Source, Saskatoon, SK S7N 2V3, Canada*
† These authors contributed equally to this work.

from the troposphere.[1–4] Stratospheric aerosols can also contain trace amounts of halogens, minerals, nitrates, mercury, and ablated metal residues from spacecraft reentry.[1,4,5] Particles in the stratosphere can persist for months to years since there are no sinks from deposition and there is limited cloud processing. As a result, they can exert a prolonged influence on Earth's radiative balance and stratospheric composition.[6–12] Therefore, their detailed chemical and morphological characterization is essential to understand their chemical, optical, and radiative properties and improve their representation in climate models.

Tropospheric material enters the upper troposphere and lower stratosphere (UTLS) *via* multiple transport pathways. The most significant is deep tropical convection across the tropical tropopause. Multiple pathways – including gradual self-lofting of smoke, synoptic-scale uplift such as in warm conveyor belts,[13] and quasi-horizonal transport such as in Asian monsoon systems[14] – are recognized as important contributors to the stratospheric aerosol budget in the midlatitudes.[11] The Dynamics and Chemistry of the Summer Stratosphere (DCOTSS) mission, however, provided unprecedented *in situ* evidence that midlatitude overshooting convection also contributes significantly to this transport.[15]

These contributions are driven by episodic intensive mesoscale convective events and display a high degree of regional variability.[6,9,16–21] Deep convective overshooting is particularly common over the continental United States during severe weather outbreaks over the summer.[22] Severe mesoscale convective systems are capable of overshooting dozens of times during their lifetime, and thousands of convective overshooting events occur each year.[23]

Early evidence of wildfire influence on stratospheric composition emerged in 1994 when trace gases from boreal fires in Canada were detected over the United Kingdom.[24] Direct observation of wildfire aerosol transport into the UTLS followed in the early 2000s during the Atmospheric Chemistry of Combustion Emissions Near the Tropopause (ACCENT, 1999–2000) and Cirrus Regional Study of Tropical Anvils and Cirrus Layers – Florida Area Cirrus Experiment (CRYSTAL-FACE, 2002) campaigns where approximately 1% of UTLS aerosol mass was identified as black carbon (BC).[19,25] Subsequent remote sensing studies of extreme wildfire events, such as the 2017 Pacific Northwest Event and the 2019–2020 Australian New Year Super Outbreak, confirmed pyroCb-driven injection of BC into the stratosphere.[8,9,20,26] The injection of wildfire smoke into the stratosphere has become an escalating concern given the increasing size, intensity, and frequency of wildfires. Across North America, wildfires have emerged as the dominant source of particulate matter (PM), decoupling regional PM trends from anthropogenic emission.[27]

Extreme wildfires can generate large anvil-shaped clouds known as pyrocumulonimbus (pyroCb), which may inject water vapor, volatile organic compounds (VOCs), and aerosol into the UTLS.[15,20,28,29] Furthermore, pyroCb smoke that does not overshoot the tropopause can gradually ascend into the lower stratosphere when sunlight warms the light absorbing organic and black carbon particles and drives self-lofting.[8,30,31] Estimates by Torres *et al.* suggest that overshooting can account for approximately 10% of total pyroCb aerosol mass injection, with the remainder self-lofting into the LS over subsequent days.[9] Deep pyroCb events can inject between 0.2–10 Gg of aerosol per event into the stratosphere depending on the severity of the fire.[13,29,32,33] With around 60 pyroCb a year,[28] even a season with just small-scale emissions injects approximately 12 Gg of aerosol into the stratosphere. This is comparable to 10% of the total sulfur aerosol injected into the stratosphere from the tropics each year. 200–300 Gg of smoke was injected into the stratosphere during major multiple pyroCb outbreaks like the Pacific Northwest Event[32,33] in 2017 and the Canadian wildfire season[13] in 2023. The effect of wildfires is more pronounced over North America.[28] It has been suggested that biomass burning organic aerosol (BBOA) may enter the stratosphere following smoke injection into the UT, then enters the LS following cross-tropopause mechanisms in the two-step process discussed by Shen *et al.*[15]

This shift is reflected in the increasing contribution of BBOA to stratospheric burdens.[15] BBOA exerts long-lasting influences on stratospheric chemistry and climate because of their extended resident times, with reported *e*-folding life-times on the order of 5 months.[6] As aerosols ascend through the UTLS, VOCs condense and contribute to particle growth, which leads to dynamic changes in their composition, morphology, optical properties, and cloud forming potential.[6,29,34,35]

The NASA DCOTSS airborne field campaign was conducted during the summers of 2021 and 2022 to investigate the impacts of deep convective transport on the composition, distribution, and evolution of stratospheric aerosols and gas species.[15,36] The mission deployed the NASA ER-2 high-altitude research aircraft, which was equipped with a suite of instruments. These included the Next Generation Particle Analysis by Laser Mass Spectrometry (PALMS-NG),[37] the DCOTSS Portable Optical Particle Spectrometer, (DPOPS),[38] a mini Multi-orifice Uniform Deposit Impactor (mini-MOUDI) for particle sampling, and multiple trace gas sensors to enable real-time measurements of aerosol properties and gas-phase species. Real-time measurements of stratospheric aerosols provide critical information about particle concentration, composition, and size distribution. However, they do not directly account for particle morphology and quantitative variations in individual particle composition, morphology and mixing state.

Computer-controlled scanning electron microscopy coupled with energy dispersive X-ray spectroscopy (CCSEM/EDX) and scanning transmission X-ray microscopy coupled with near-edge X-ray absorption fine structure (STXM/NEXAFS) spectroscopy has been shown to be an effective methodology to assess the size, morphology, composition, and mixing states of BBOA particles, which provide critical experiment data to model aerosol optical and radiative properties.[39–46] In this study, we extend prior DCOTSS findings[15] by reporting detailed chemical imaging observations of individual stratospheric particles sampled during the 2022 mission flights conducted from deployment bases in Salina, Kansas and Palmdale, California. These flights probed a range of stratospheric conditions over the continental United States and the Eastern Pacific, and

provided new insights into the spatial variability, composition, and wildfire influence on stratospheric aerosol populations.

Experimental

Research flights, particle sampling and measurements

This study presents chemical imaging results of stratospheric particles collected during six research flights conducted in June and July 2022 as part of the DCOTSS airborne field campaign. All flights were conducted aboard the NASA ER-2 high-altitude research aircraft. Fig. 1A shows the influence of overshooting outflow along the DCOTSS flight tracks and active fires five days before and during the DCOTSS campaign (June 1, 2022–July 12, 2022) observed by the Moderate Resolution Imaging Spectroradiometer (MODIS).[47] Areas of "active convection" refer to flight segments where water vapor concentrations were substantially elevated relative to the local background and coincided with ongoing overshooting convection. Flight segments of "recent convection" are defined by water vapor enhancements associated with overshooting convection less than 1.5 days old *via* colocation with overshoot air trajectory calculations, while "aged convection" corresponds to overshooting convection that occurred more than 1.5 days ago. Flight segments labeled as "aerosol layer" and "unknown hydration" represent areas with enhanced aerosol or water vapor signals, respectively, that do not align with computed trajectory paths of prior convection events.[48] Underlaying maps in Fig. 1 display fire detection data derived from MODIS satellite observations.[47] Fire pixels with observed brightness temperature exceeding 400 K compared to the surrounding 21 × 21 pixel grid were classified as severe fires and are marked with fire icons, while those with brightness temperature below 400 K are indicated with red dots.[49]

Four flights (RF15, RF17, RF18, and RF19) were conducted over the continental United States, and two flights (RF21 and RF23) were flown over the Pacific Ocean. The flights are categorized into two groups: survey flights (RF15, RF18, and RF21), which sampled mostly background stratospheric conditions, and convection flights (RF17, RF19, and RF23), which targeted regions influenced by recent and aged convective overshooting outflow. Particle number concentrations and size were measured in real time by DPOPS, while particle type and chemical composition were characterized by PALMS-NG. Particle number concentrations during each flight are shown in SI Note 1 (Fig. S1). These instruments provided comprehensive *in situ* characterization of aerosol number concentrations, size distributions, and particle-type composition. Additional technical details regarding both instruments during the DCOTSS campaign can be found in Shen *et al.*[15] and Li *et al.*[38]

UTLS particles were collected for offline analysis using a model 135–10B Mini-Multi-Orifice Uniform Deposit Impactor (Mini-MOUDI) operated at a flow rate of 2 L min^{-1}. Samples were impacted on stage 5, with a nominal aerodynamic size range of 1.8–3.2 μm. Two types of microscopy substrates were used: copper 400 mesh TEM grids coated with carbon type-B thin film (Ted Pella, Inc.), and 100 nm thick Si_3N_4 windows supported by silicon frames (Silson Ltd). A single set of samples was collected per flight, so the offline analysis represents the average of the period when mini-MOUDI was open. The single particle analysis for the survey and convective flights reflects the overall flight path; however, it is biased toward lower stratospheric altitudes. Convective flights are heavily influenced by recent convective activity at low stratospheric altitudes as well. Particle sampling was mainly at stratospheric altitudes with automated ambient pressure valve control. The fraction of stratospheric aerosols collected is shown in Table 1. Open and close pressure thresholds were set prior to takeoff based on the tropopause height forecasted with version 5 of the European Centre for Medium-Range Weather Forecasts (ECMWF) reanalysis, ERA5.[50] Overshooting cloud tops were identified with ground-based radar and satellite observations.[23,51] After collection, the TEM grids were stored in grid storage boxes and the Si_3N_4 windows were stored in the original capsules, which were then stored in plastic tubes, sealed with Parafilm, placed in Ziplock bags with silica gel desiccant, and kept in desiccator cabinets until analysis.

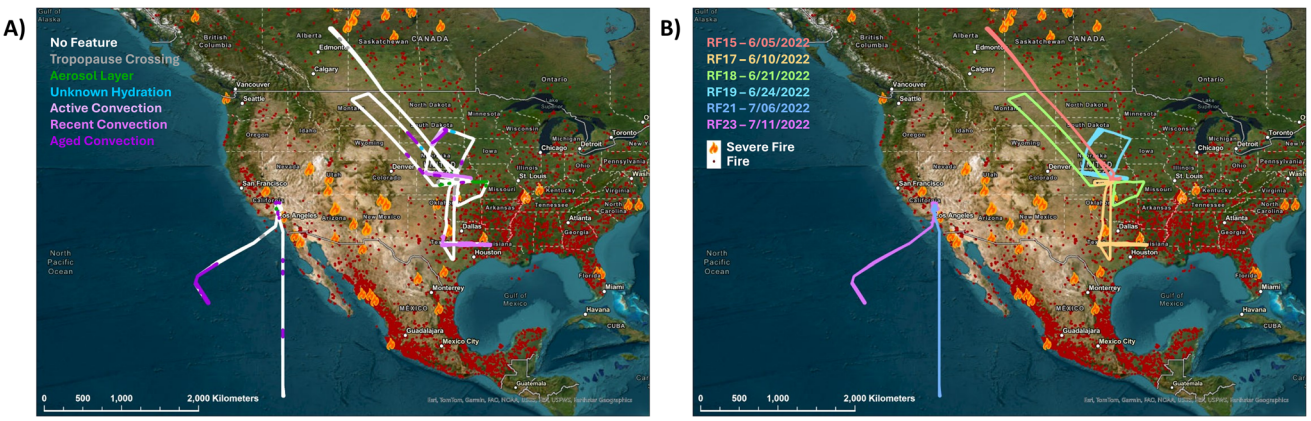

Fig. 1 DCOTSS research flight trajectories, overshooting outflow influence, and active fire locations. (A) Influence of convective overshooting outflow and other features along flight trajectories and MODIS observed active fires from June 1, 2022–July 21, 2022. (B) Research flight trajectories color-coded based on research flight.

Table 1 Mini-MOUDI sampling parameters, DPOPS number concentrations while the mini-MOUDI, PALMS-NG BBOA number fraction, PALMS-NG organic mass fraction, percent of particle sampled in the stratosphere, and number of particles analyzed with CCSEM/EDX and STXM/NEXAFS for each flight. Particle data from DPOPS and PALMS-NG was only considered when the mini-MOUDI was open

Flight	RF15	RF17	RF18	RF19	RF21	RF23
Date	6/5/22	6/10/22	6/21/22	6/24/22	7/6/22	7/11/22
Open P (mBar)	140	150	160	160	100	140
Close P (mBar)	145	155	165	165	105	145
Potential T (K)	>385	>370	>357	>365	>410	>370
Ozone (ppb)	>400	>100	>100	>110	>500	>180
DPOPS average particle concentration (#/cm^3)	3.98	4.32	4.02	3.67	2.87	4.75
DPOPS Max particle concentration (#/cm^3)	10.28	8.70	38.24	14.38	10.04	11.19
PALMS-NG BBOA number fraction	0.32	0.41	0.21	0.43	0.10	0.38
PALMS-NG organic mass fraction	0.46	0.62	0.34	0.56	0.14	0.57
% Stratospheric	100%	98%	91%	99%	100%	98%
CCSEM/EDX particles	1495	3680	1267	1627	3080	3865
STXM/NEXAFS particles	421	972	247	608	228	389

Scanning electron microscopy

Elemental analysis of individual particles was performed using computer-controlled scanning electron microscopy coupled with energy dispersive X-ray spectroscopy (CCSEM/EDX). Measurements were performed on a Quanta FEI 3D SEM operated at 20 kV, equipped with an EDAX Genesis EDX spectrometer at the Pacific Northwest National Laboratory. Particles were automatically detected with an area equivalent diameter (AED) threshold of 100 nm to 3.5 μm. For each particle, individual EDX spectra were acquired to determine elemental composition.[40,52] The spectra were processed to quantify the relative abundance of 14 elements commonly present in atmospheric particles: C, N, O, Na, Mg, Al, Si, P, S, Cl, K, Ca, Mn, Fe, and Cu. Elemental fractions of copper (Cu) were then excluded from the data analysis due to its background signal originating from the TEM grid. Elemental fractions of C, O, and N are regarded as semi-quantitative, due to contributions from the thin film substrate along with other experimental complications.[53] However, their semi-quantitative values and association with other elements in particles are practically used for cluster analysis. Particle classification was performed using K-means clustering, an unsupervised machine learning algorithm that partitions data into clusters by minimizing the within-cluster variance. Three clusters were selected for this analysis. Further methodological details are provided in SI Note 2. In addition, to account for deformation or spreading upon substrate impact, particle sizes determined as area equivalent diameter (AED) in microscopy images were converted to corresponding spherical equivalent diameter (SED) using geometrical correction procedure[54] illustrated in SI Note 3. Particles with SED values smaller than 100 nm were excluded from the dataset to maintain consistency in detection limits and analytical reliability.

X-ray microscopy

Scanning transmission X-ray microscopy with near-edge X-ray absorption fine structure (STXM/NEXAFS) spectroscopy was used to spatially resolve the chemical bonding environment and oxidation state of carbon within individual particles. STXM experiments were conducted at two synchrotron facilities: beamline 5.3.2.2 at the Advanced Light Source (Lawrence Berkely National Laboratory, Berkeley, CA, USA) and beamline 10ID-1 at the Canadian Light Source (Saskatoon, SK, Canada). In STXM/NEXAFS experiments, the sample is raster-scanned through a focused X-ray beam while collecting image stacks at multiple photon energies across the carbon K-edge spectral region so that each pixel contains X-ray absorbance information.[44,55,56] For rapid compositional mapping, fast carbon maps were generated using four key energies: 278 eV (pre-edge baseline), 285.4 eV (C=C), 288.5 eV (COOH), and 320 eV (post-edge baseline).[44,56] These maps allow differentiation of elemental carbon (EC, *e.g.* soot), organic carbon (OC), and inorganic (IN) components.[56–58] The organic volume fractions (OVF) of particles was calculated by quantifying the thickness of the OC, EC, and IN components on a per-pixel basis.[39,45,59,60] In this analysis, ammonium sulfate as assumed to be the dominant IN component, while adipic acid was used as a proxy for OC due to its oxygen-to-carbon (O : C) ratio of 0.66, which is representative of aged organic aerosol.[61]

Metrics of particle diversity and mixing state were also derived from STXM/NEXAFS data to assess internal heterogeneity. Detailed protocols for image acquisition, alignment, and spectral processing have been reported prior publications[39,40,60,62] and summarized in SI Note 4, Consistent with CCSEM/EDX analysis, particles with SED values less than 100 nm were excluded from analysis to ensure measurement accuracy and comparability across techniques.

Results and discussion

Flight descriptions and sampling summary

Prior to each flight, tropopause pressure was forecasted, and the resulting values were used to define ambient pressure thresholds for activating the sampling valve. At the conclusion of each flight, the height of the tropopause was determined across the

flight track to determine the percent fraction of particles that were sampled in the stratosphere. Table 1 summarizes key parameters for each flight, including the flight date, mini-MOUDI open and close pressure thresholds, recorded low-limit values of potential temperature and ozone concentration during sampling, average and maximum particle number concentrations, PALMS-NG BBOA number fraction, PALMS-NG organic mass fraction, the percent fraction of particles sampled in the stratosphere, and the number of particles analyzed by CCSEM/EDX and STXM/NEXAFS. Potential temperature and ozone concentrations were used to verify that particle sampling occurred within the stratosphere. Potential temperature is the temperature an air parcel would attain if adiabatically brought to a standard pressure of 1 atm. Typical tropopause potential temperatures range from approximately 370 K near the equator to 340 K near the poles.[63] The percent fraction of stratospheric particles (%Stratos) in each flight-averaged sample was calculated as the ratio of the total number of particles counted by DPOPS above the tropopause to the total number of particles counted over the entire flight duration, as defined in eqn (1). DPOPS particle counts were included in the analysis only during periods when the mini-MOUDI sampler was actively collecting. High values of this metric (ranging from 91% to 100%) confirm that the majority of particles analyzed offline were collected under stratospheric conditions.

$$\%\ \text{Stratospheric} = \frac{\text{DPOPS}_{\text{stratos}}}{\text{DPOPS}_{\text{total}}} \times 100\% \quad (1)$$

Across all flights, aerosol number concentrations were typically highest near the tropopause and decreased with altitude. As shown in Table 1, all flights sampled more than 98% stratospheric aerosols with the exception of RF18 which sampled 91% stratospheric air. Here, the highest particle concentrations generally occurred near the tropopause and often overlaps with regions influenced by convection. Particle data from DPOPS and PALMS-NG were only considered during periods when mini-MOUDI was open. The average DPOPS number concentration across all flights was 3.96 ± 1.44. The average PALMS BBOA number fraction was 0.31 ± 1.3 and the averaged organic mass fraction was 0.45 ± 0.19. Both convection-targeted and survey flights sampled substantial amounts of background stratospheric air, making it difficult to isolate the direct impact of convective events on aerosol composition.

RF15 surveyed high latitudes and altitudes during which PALMS-NG recorded BBOA number fraction of 0.38 and an organic mass fraction of 0.46 ± 0.31 at stratospheric altitudes. DPOPS measured an average particle number concentration of 4.0 cm^{-3} and there was no major variation in particle concentration across the flight caused by deep convection. During the sampling period, the potential temperature remained above 385 K and ozone concentrations exceeded 400 ppb. All particles sampled during RF15 by mini-MOUDI were in the stratosphere based on the measured tropopause height.

RF17 targeted convective outflow over eastern Texas and recorded strong biomass burning signals. PALMS-NG reported a BBOA number fraction of 0.41 and an organic mass fraction of 0.62 ± 0.24. DPOPS recorded an average particle number concentration of 4.3 cm^{-3}, with the highest concentrations (up to 8.7 cm^{-3}) near the tropopause during transits through the regions affected by recent convection (Fig. 1). The sampling by mini-MOUDI was activated at potential temperatures above 370 K and ozone levels exceeding 100 ppb. Some tropospheric air was sampled at the start and end of the flight. However, 98% of collected particles were in from the stratosphere.

RF18 conducted surveying and vertical profiling of the central region of the North American monsoon stratospheric anticyclone, with a secondary objective of intercepting a pyroCb smoke plume just below the tropopause.[21] PALMS-NG BBOA number fraction was 0.21 with an organic mass fraction of 0.34 ± 0.34. DPOPS recorded an average particle number concentration of 4.0 cm^{-3}, with the largest values near the tropopause (up to 38.2 cm^{-3}) and decreasing to 1.4 cm^{-3} with altitude. Mini-MOUDI operated above 357 K potential and ozone concentration above 110 ppb. However, it was not active during the peak BBOA signal within the pyroCb smoke detected by PALMS-NG. Approximately 91% of particles were sampled in the stratosphere.

RF19 targeted both convective outflow over Nebraska and South Dakota, and an 18 h old overshooting cloud top over Kansas. PALMS-NG reported the highest BBOA number fraction of all six flights at 0.43 and high organic mass fractions at 0.56 ± 0.25. The DPOPS recorded an average particle number concentration of 3.7 cm^{-3}, with concentrations observed over northern Kansas between 1.5–14.4 cm^{-3} and 1.6–14.5 cm^{-3} observed over South Dakota (SI Note 1, Fig. S1). Sampling was activated above 365 K potential temperature with ozone concentrations greater than 100 ppb. Some tropospheric air was sampled by mini-MOUDI at the beginning and end of the flight. As a result, 99% of sampled particles were in the stratosphere, and all particles sampled inside regions influenced by active and recent convection were in the stratosphere.

RF21 surveyed background free stratospheric aerosol in the subtropical stratosphere. PALMS-NG detected a low BBOA and organic signal, 0.10 and 0.14 ± 0.22 respectively. DPOPS measured the lowest average particle number concentration across all flights, averaging 2.9 cm^{-3}. Particle variation during this flight corresponded to changes in altitude. Mini-MOUDI was activated at 410 K potential temperature and ozone concentrations were above 500 ppb. In this flight, 100% of sampled particles were from the stratosphere.

Finally, RF23 sampled 3 days old overshooting material over the Pacific Ocean, transported from the Sierra Madre region. PALMS-NG reported a BBOA number fraction of 0.38 and an organic mass fraction of 0.59 ± 0.29. DPOPS recorded the highest average particle number concentration of 4.8 cm^{-3}, with the majority of particles sampled from the region influenced by aged convection where particle number concentrations were in the range of 8–12 cm^{-3}. Mini-MOUDI operated at potential temperatures and ozone concentrations above 370 K

and 180 ppb, respectively. As a result, 98% of collected particles were stratospheric.

Elemental composition and particle size

CCSEM/EDX analysis of particles sampled across all DCOTSS flights reveals consistent elemental composition and size-resolved classification. Fig. 2 presents the three distinct size-resolved cluster assignments derived from K-means clustering. Clusters 1 and 2 are primarily composed of C, O, Si, and S, with minor contribution from N. Cluster 2 has greater contribution from Si and S compared to cluster 1 but otherwise share the same elements (SI Note 2, Fig. S2). The elevated C fractions in these clusters are influenced by the thin-film substrate and may not directly reflect particle composition. Nonetheless, S dominated particles like those in Clusters 1 and 2 are consistent with previously reported stratospheric aerosol composition.[2,3,11,20,25] Due to their composition, these clusters are defined as organic influenced sulfates 1 & 2, and negative silhouette scores for some particles assigned to cluster 2 indicate a compositional continuum between the organic influenced sulfate clusters. Cluster 3 exhibits distinct Mg, Al, and Fe peaks in addition to the elements common in the other clusters. This is consistent with influence from ablated meteoritic and spacecraft materials, and the sulfate-coated meteoric and biomass burning materials observed by PALMS-NG.[4,15] As a result, Cluster 3 is defined as particles influenced by inorganic ablation. Inorganic ablation particles from Cluster 3 dominate the largest particle sizes, while particles with SED < 0.3 μm are dominated by organic influenced sulfates. Some of the high carbon features in the smallest size bins may be caused by organic particles shattering upon impact with the substrate (Fig. 2B). The overall elemental profiles observed here are broadly consistent with the known stratospheric aerosol composition.[2,3,11]

Particle carbon content speciation

STXM/NEXAFS imaging was used to investigate carbon speciation, particle morphology, and internal mixing state of individual stratospheric aerosol particles. Carbon K-edge absorption spectra enabled the identification of three primary components: organic carbon (OC), which represents non-refractory carbonaceous material; elemental carbon (EC), which represents graphitic or soot-like structures; and inorganic (IN) material, which encompasses non-carbonaceous constituents such as sulfates and ablated metals. Unlike CCSEM/EDX, STXM/NEXAFS does not resolve inorganic species

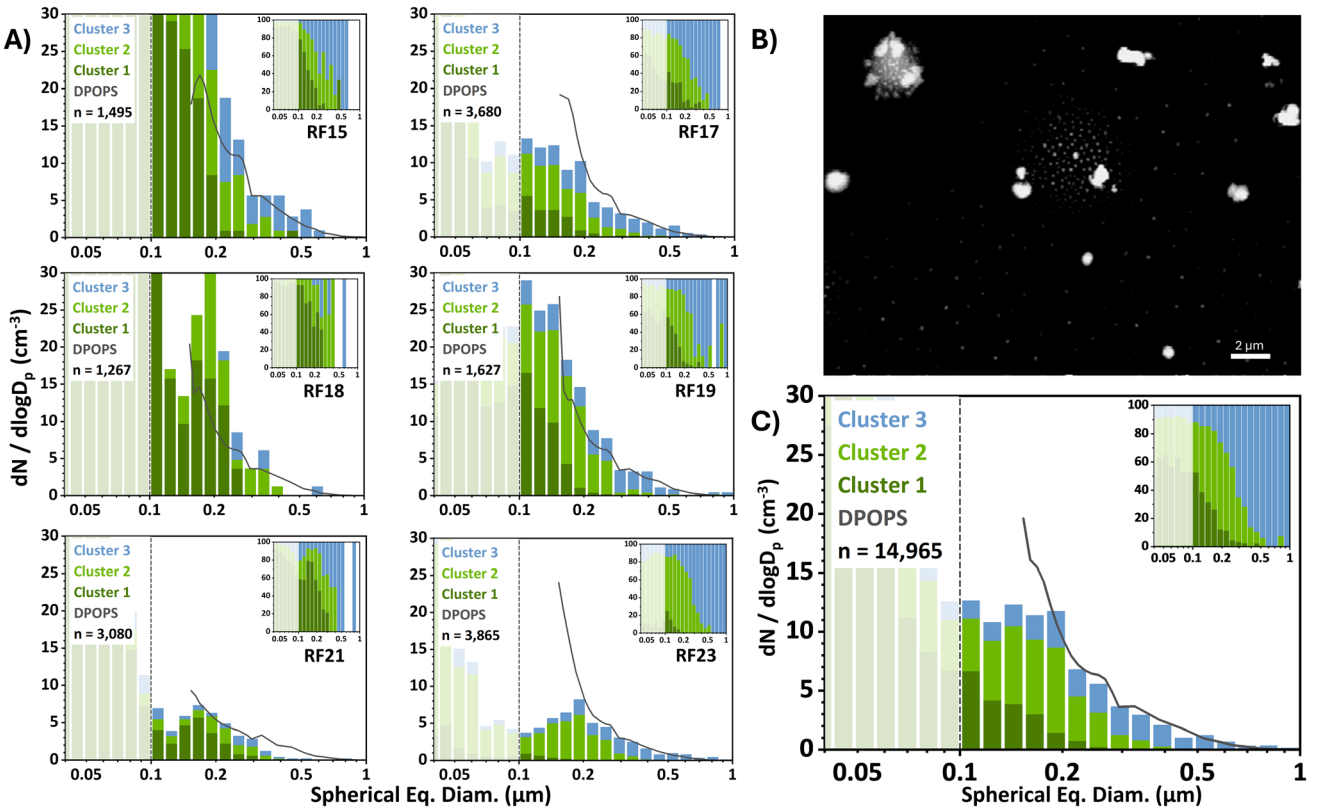

Fig. 2 Size resolved clustered elemental compositions of individual particles derived from CCSEM/EDX analysis, presented as 16 bin per decade histograms. Clusters 1 and 2 represent organic-influenced sulfate particles. Cluster 3 contains particles influenced by inorganic ablated materials. (A) Particle size distributions of each flight, normalized to the *in situ* number concentration measured by DPOPS at 0.3 μm (grey line). Particles with spherical-equivalent diameters smaller than 0.1 μm are shown in shaded tones and are likely influenced by contributions from shattered debris; therefore, they are excluded from further discussion. (B) Representative SEM image that shows particle morphology and an example of particle shattering (center) from RF17. (C) Combined particle size distributions from all six flights, normalized to the average DPOPS number concentration.

at the photon energies used, instead it categorizes them collectively as IN components.

Fig. 3A presents particle carbon speciation classifications for each flight as size-resolved histograms, normalized to the *in situ* DPOPS number concentrations at 0.3 μm. To assign these classifications, individual particles were categorized into five carbon speciation groups (OC, OCIN, IN, OCEC, and OCECIN) following established criteria from previous works.[39–41,56,60,64] These categories reflect the degrees of internal mixing between carbonaceous and inorganic material within particles. Fig. 3B shows a representative carbon speciation map, where pixel color indicates the dominant component: OC (green), EC (red), or IN (blue). These maps illustrate that many particles exhibit complex internal mixing that comprise OCIN, OCEC, and OCECIN groups. Across all flights, 89% of analyzed particles contained OC, with OCIN as the most prevent group (Table S1). Smaller particles were more frequently classified as OC or IN, while OCIN dominated the mid-size range of the distribution. EC-containing particles accounted for approximately 5% of the total population and were primarily classified as internally mixed OCECIN. These particles were commonly observed in flights targeting convective outflow (RF17, RF19, and RF23), although EC was also detected in background stratospheric conditions during the survey flights (RF15, RF18, and RF21). The presence of EC-containing particles in the survey flights suggests that biomass burning contributes to the stratospheric OC pool (see SI Note 4, Table S1). The high degree of internal mixing observed in EC-containing particles is consistent with soot produced by biomass burning events.[20,29] Furthermore, spectral features characteristic of potassium, a biomass burning tracer,[65] were clearly observed in 18% of the NEXAFS spectra (Fig. S5). However, the potassium mass fraction in individual particles was likely below 0.5%, – the low detection limit of CCSEM/EDX particle analysis. As a result, potassium was detected by EDX only in occasional particles.

Fig. 4 presents the size-resolved distributions of organic volume fraction (OVF) derived from STXM/NEXAFS carbon maps. All 2865 particles analyzed by STXM showed the presence of organic carbon. To maintain consistency with the carbon speciation classifications described above, particles with OVF values below 0.1 were categorized as IN. Overall, 97% of particles have OVF values greater than 0.1. The most common range is 0.2–0.4 (45% of particles), followed by 0.4–0.6 (20% of particles) and 0.1–0.2 (16% of particles), as shown in SI Note 4, Table S2 and Fig. S6.

The campaign-wide average OVF is 0.37 ± 0.20. These values are in qualitative agreement with concurrent PALMS-NG measurements, which report an organic mass fraction ranging from 0.3 to 0.6. Despite inherent differences in measurement techniques, both STXM and PALMS-NG data consistently

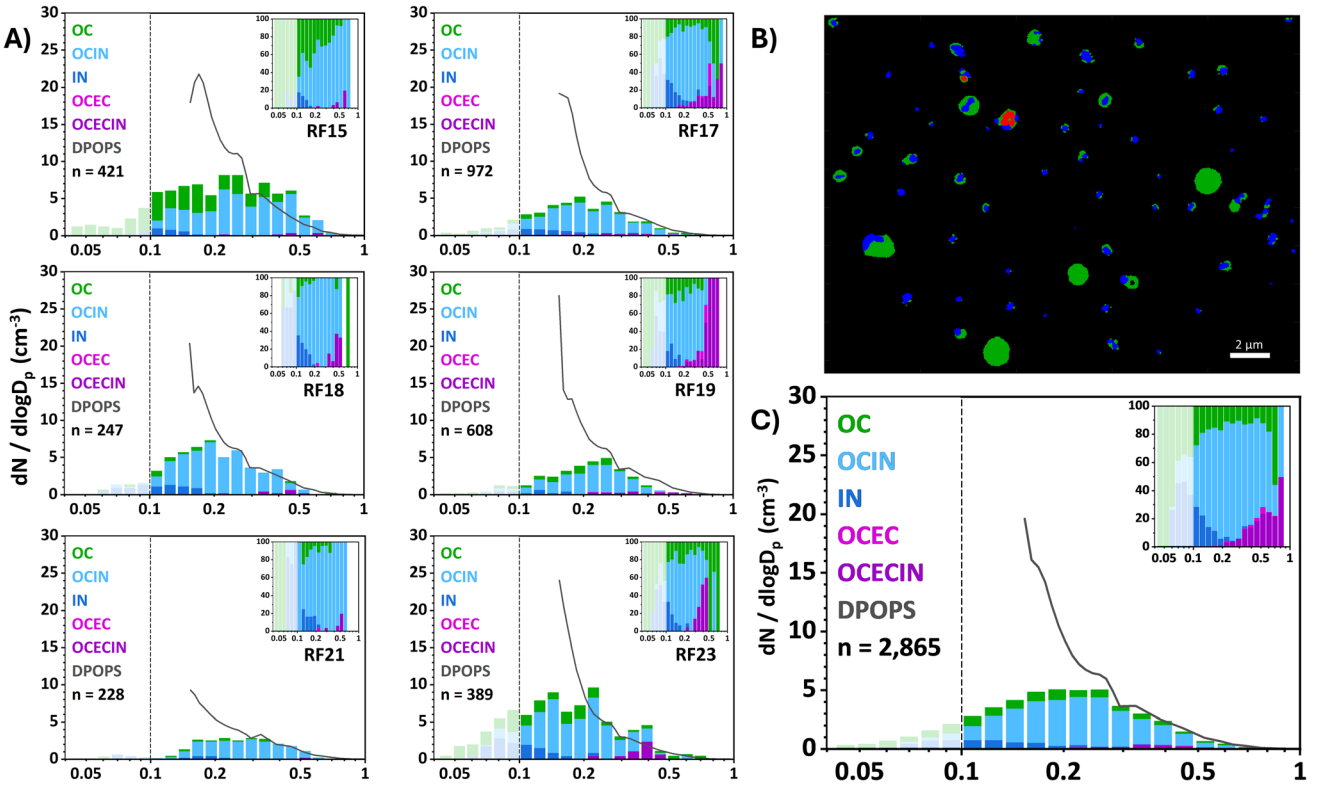

Fig. 3 Size-resolved carbon speciation classifications of individual particles derived from STXM/NEXAFS carbon speciation maps. (A) Particle size distributions for each flight, shown as 16 bin per decade histograms, normalized to the number concentration measured by DPOPS at 0.3 μm (grey line). (B) Representative carbon speciation map from RF17. Pixel colors indicate the dominant component: organic carbon (OC, green), elemental carbon (EC, red), and inorganic components (IN, blue). (C) Combined particle size distribution for all size flights, normalized to the average DPOPS number concentration at 0.3 μm.

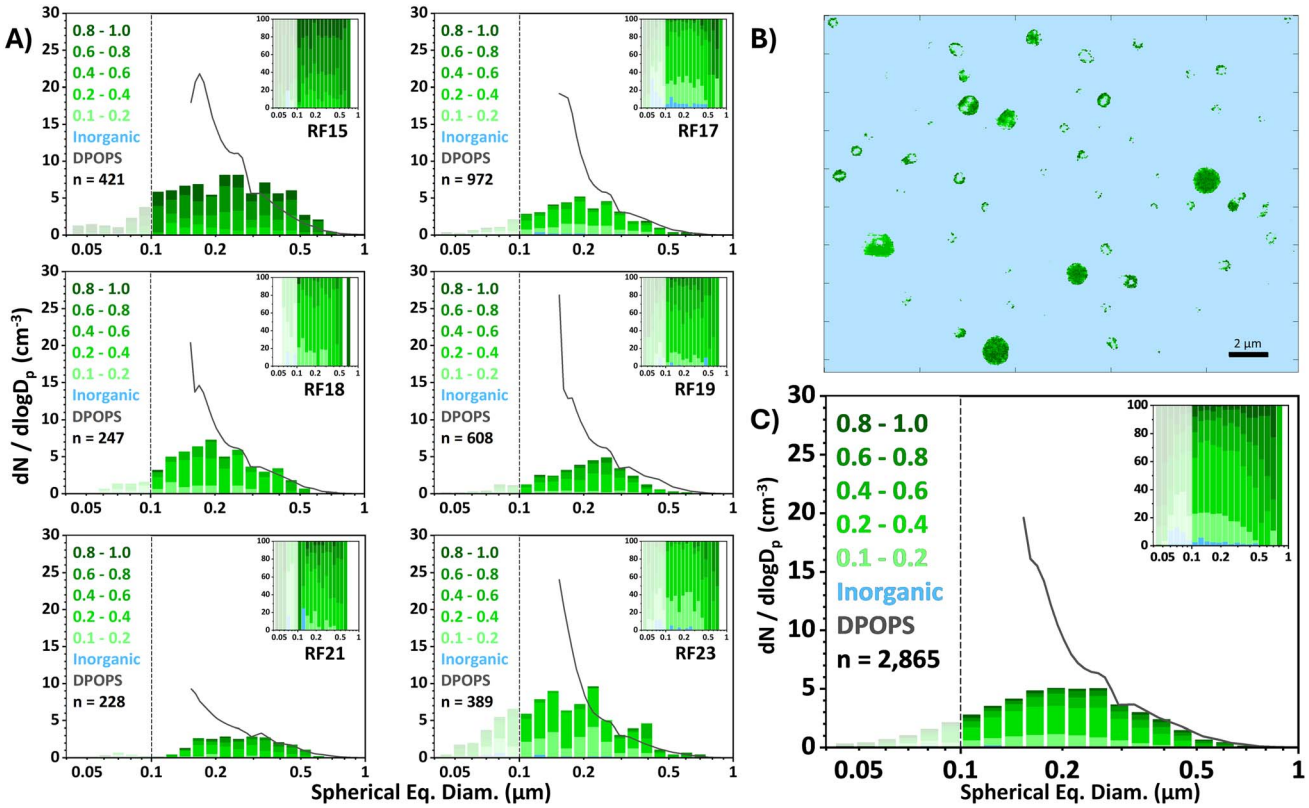

Fig. 4 Size-resolved organic volume fractions (OVF) of individual particles derived from STXM/NEXAFS carbon speciation maps. (A) Particle size distributions for each flight, displayed as 16 bin per decade histograms normalized to the DPOPS-measured number concentration at 0.3 μm (gray line). (B) Representative OVF map from RF17, where pixel colors correspond to the OVF ranges shown in the legends. (C) Combined particle size distribution of all six flights, normalized to the average DPOPS number concentration at 0.3 μm.

indicate elevated contributions of organic components in stratospheric particles. OVF values spanned a wide range across the analyzed particles, with pure IN (OVF = 0.00) particles and some pure OC particles (OVF = 0.99). Particles smaller than 0.1 μm show a slight increase in OVF, which is attributed to shattering of OC-rich fragments from larger particles upon impact with the substrate, as seen in an SEM image in Fig. 2B. Across the observed size range, OVF values generally increase with particle size and are correlated with the occurrence of EC-containing particles. Since EC thickness is explicitly accounted for in the OVF calculation, this trend suggests that organic material condensed onto pre-existing EC-particles, which is consistent with other observations of BBOA sampled from wildfire emissions.[6,21,29,66] Among all flights RF15 exhibited the highest number of pure OC particles, and the highest average OVF (0.65 ± 0.18). When RF15 is excluded from the dataset, the average OVF decreases to 0.33 ± 0.17. The elevated organic content observed in RF15 remains unexplained, but may be influenced by seasonal factors, the origin of the sampled air mass, or higher ozone concentrations along the flight track.[1,16,67]

Particle morphology

STXM-derived component maps were used to investigate particle morphology and infer formation pathways based on the internal arrangement of OC, EC, and IN components within particles. In particular, the spatial distribution of OC relative to IN provides insight into whether particles formed *via* condensation or coagulation processes. Furthermore, the internal mixing of OC and EC significantly influences aerosols optical properties. To quantify particle morphology, the centroid position of each component (r_c) was calculated relative to the maximum radial extent of a particle (r_{max}), defined as the distance from the geometric center to the outermost edge. For each component i, the radial offset centroid distance, expressed as $R_i = r_c/r_{max}$ ratio, ranges from 0 (fully centered) to 1 (maximally offset). Centroid positions were weighted by pixel optical density to better represent the mass distribution of each component within the particle.

Fig. 5 displays the OVF weighted $R_{OVF} = r_c/r_{max}$ ratios calculated for OC components within the OCIN particle groups and indicates an overall trend of core (IN) – shell (OC) morphology. In ideal core–shell morphology, the centroid of the shell-forming OC coincides with the particle center, which results in a distance ratio close to 0.[68] A particle with an IN shell with an OC core would also return a distance ratio close to 0; however, inspection of particle images did not reveal particles with OC cores. Conversely, higher ratios indicate partial separation or asymmetric mixing of components. Resolution of this analysis was improved by weighing OC pixels by their corresponding OVF values to account for the gradient of mixing with IN. The average R_{OVF} for OCIN particles was 0.13, indicating that

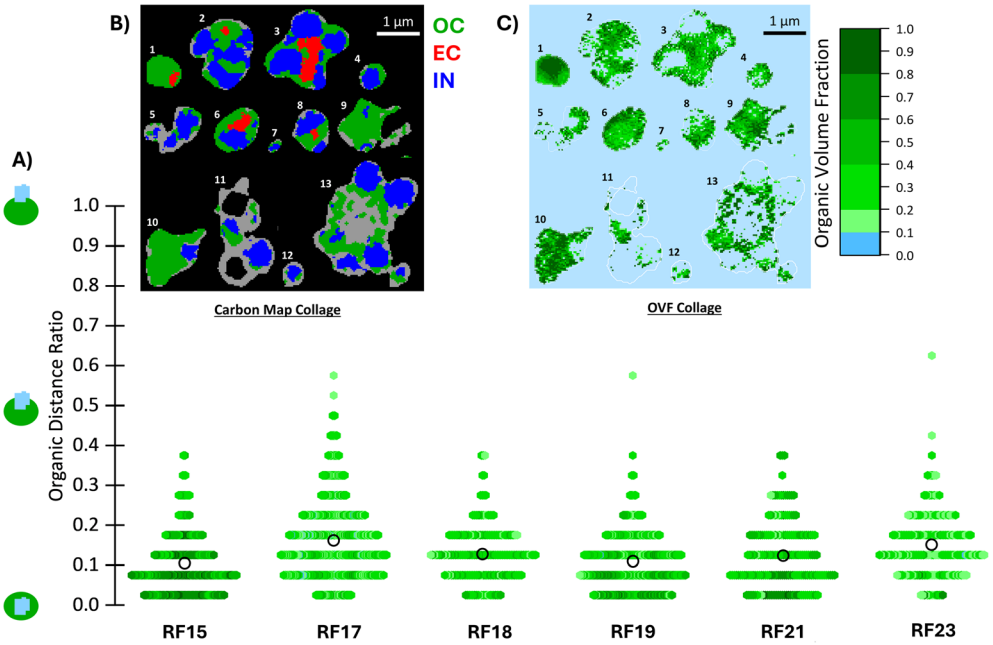

Fig. 5 (A) Radial offset centroid distance ratios (R_{OVF}) of OC components in OCIN particle from each flight. Black circles indicate the average distance ratio per flight. The overall average distance ratio across all particles as 0.13 ± 0.01, consistent with OC forming an external phase that engulfs IN cores. (B) Representative carbon speciation maps of individual particles from RF15 that show spatial distributions of OC, EC, and IN components. The numbers indicate particle IDs. (C) Corresponding OVF maps for the same particles shown in (B) that highlight the internal variation in organic component. Distance ratios of R_{IN}, R_{OC}, and R_{EC} for individual particles in the maps are provided in SI Note 4, Table S3.

IN is general engulfed by an OC-rich phase. The dominance of low R_{OVF} distance ratios, and the lack of values approaching unity, supports a formation mechanism in which OC components in particles primarily result from gas-to-particle condensation on preexisting particles, rather than coagulation of externally mixed particles.

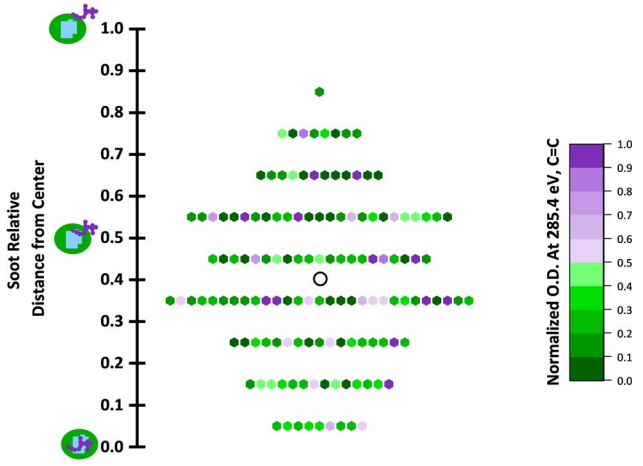

Fig. 6 Radial offset centroid distance ratios R_{EC} of EC components in all EC-containing particles (OCEC and OCECIN groups) from all flights. The overall average ratio across all particles is 0.40 ± 0.02 (marked by black circle), suggests that EC is predominantly encapsulated by OC and positioned near the surface of underlying IN inclusions. Each hexagon represents an EC-containing particle color coded by the normalized optical density at 285.4 eV (C=C).

Fig. 6 presents the radial offset centroid distance ratios R_{EC} for EC-containing particles (OCEC and OCECIN groups), which provide insight into the internal positioning of soot relative to the particle center. Among the 2865 particles analyzed by STXM, approximately 5% contained identifiable EC inclusions, with an average distance ratio of $R_{EC} = 0.4 \pm 0.02$. This intermediate value suggests that soot is typically embedded with the particle but offset from the center – frequently positioned on or near the surface of IN-rich cores and surrounded by an organic carbon (OC) shell. This EC/OC/IN configuration implies a partially engulfed morphology in which EC is internally mixed but not deeply buried. Interestingly, R_{EC} values observed for stratospheric particles are higher than those previously reported for freshly emitted BBOA. This may be attributed to the higher fraction of IN components within stratospheric particle cores, as well as the occurrence of liquid–liquid phase separation within the organic shells of EC-containing particles – a trend previously observed in BBOA during tropospheric field campaigns.[69,70] Such phase separation is likely to occur within the plume during its early evolution, when relative humidity (RH) is high and organic components begin to condense onto mixed-phase cores. At stratospheric altitudes, reduced RH and cold temperature may limit further phase mixing, potentially preserving these core–shell structures during long-range transport. Further work to assess particle viscosity at stratospheric conditions is needed to adequately assess EC-OC distributions in individual particles. This internal mixing state information has important implications for aerosol optical properties. Particles with internally mixed EC and OC can exhibit enhanced light absorption due to lensing effects, compared to externally mixed or bare soot particles.[34,71,72] Core-shell

morphologies of EC-containing particles is consistent with tropospheric biomass burning emissions, stratospheric pyroCb emissions from the 2019 Williams Flats fire imaged by Beeler *et al.*, and the condensation of OC onto existing particles in pyroCb observed by Gorkowski *et al.*[29,34,73]

Particle mixing state and composition

Particle mixing state offers an additional metric for understanding both optical properties and formation pathways. Using the component thickness maps from STXM/NEXAFS, the mass fractions of OC, EC, and IN were estimated on a per-particle basis, as described in SI Note 4. Averaged across all six flights, particles consisted of approximately 32% OC, 1% EC, and 67% IN by mass. Similar to OVF measurements, there was a wide range of particle mass fractions, with OC and IN ranging between 0–100% and EC ranging between 0–69%. The average OC mass fraction is consistent with the observed OVF and the average EC fraction aligns with previously reported BC levels associated with aged BBOA material.[6] However, substantial variability in component mass fractions was observed across flights. The survey flights (RF15, RF18, and RF21) exhibited lower EC mass fractions than the active convection flights (RF17, RF19, and RF23). This likely reflects increased atmospheric processing and dilution following initial convective injection (SI Note 4, Table S4). Notably, RF15 displayed significantly higher OC mass fractions than any other flight. When RF15 is excluded from the average, the mean OC mass fraction decreases to 26% while the IN fraction increases to 73%. The campaign-wide EC fraction remains largely unchanged.

Mass fraction estimates of OC, EC, and IN components also enable the quantification of individual particle diversity.[39,60,62] This diversity metric, D_i, ranges from 1 to the total number of components present (3 in the case of OC, EC, and IN). A D_i value of 1 indicates a single-component particle while a mixed-component particle with equal fractions of all components yields a D_i value of 3. Stratospheric aerosols are generally dominated by OC and IN, and results in a limited variability in D_i across most flights shown in Fig. S7.

Particle mixing state is more comprehensively represented by plotting bulk sample diversity, D_γ, against the average particle diversity, D_α. Here, D_γ, reflects the number of distinct components across the entire sample, while D_α quantifies the average number of components per particle. These two parameters define D_γ *versus* D_α space, which is used to calculate the mixing state index (χ), a metric that characterized the extent of external *vs.* internal mixing.[60,62,74,75] Fig. 7 shows that all flights exhibit similar D_γ values, which reflects consistent sample-wide particles composed of OC and In, with trace contributions from EC. RF15 and RF21, the northern and tropical survey flights, display higher D_α values, which indicates more internal mixing in background particles. These flights sampled primarily overworld stratosphere (>380 K potential temperature) while RF17, RF19, and RF23 sampled near the tropopause and might be more aged aerosol. In general, the mixing state index χ is consistent across all flights, which suggests the overall mixing state of stratospheric aerosol is consistent between the background and convectively influenced regions.

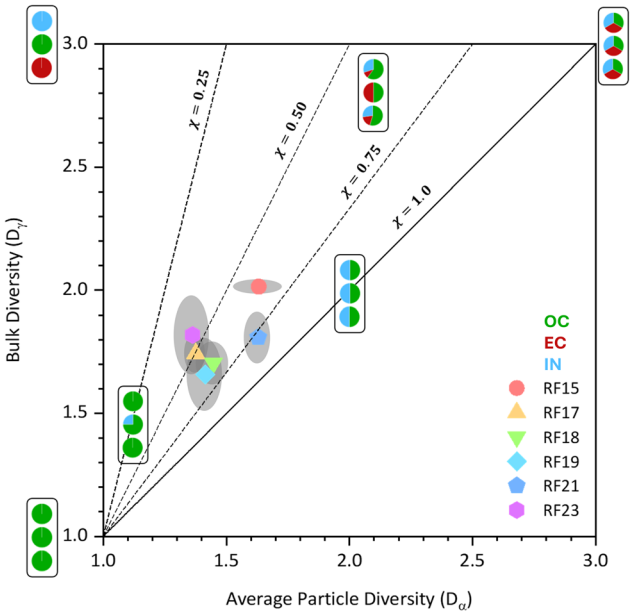

Fig. 7 Mixing state diagram showing bulk diversity, D_γ, plotted against average particle diversity, D_α, for each flight based on STXM-derived mass fractions of OC, EC, and IN. Shaded regions indicate the uncertainty in both diversity parameters. Dashed lines represent mixing state index, χ, thresholds adapted from Riemer and West (2013).[74] Six example particle populations are illustrated, each showing three particles with varying component mass fractions to visualize differences in internal mixing.

Conclusions

This study characterized the composition and morphology of stratospheric particles collected during six research flights over North America as part of the summer 2022 DCOTSS campaign. Particles were impacted onto TEM grids and silicon nitride substrates for multi-modal chemical imaging utilizing CCSEM/EDX and STXM/NEXAFS. The analysis revealed that the smallest particles (0.1–0.3 μm) are dominated by organic-influenced sulfates, while larger particles (0.3–1.0 μm) exhibited enrichment in inorganic elements indicative of meteor and spacecraft ablation. X-ray imaging shows that 89% of particles contained a significant OC component, and 5% contained internally mixed EC, consistent with previous observations of biomass burning aerosol injected into the stratosphere by deep convective events from severe wildfires.[6,7,20,29,34] OVF values exceeded 0.1 in 97% of particles, with an average OVF of 0.37 across all flights. Higher OVF values were observed in particles containing EC, particularly during flights that sampled convective outflow. These results suggest that OC components in stratospheric particles can be attributed to BBOA, most likely from recent intense wildfires and deep convective events, although the relative contribution from different transport pathways remains uncertain.[15]

Particles classified as OCIN and OCECIN exhibited core–shell morphologies consistent with the condensation of OC onto pre-existing IN and EC cores. Component mass fractions were also quantified, with particles averaging 32% OC, 1% EC,

and 67% IN by mass. EC mass fraction values are consistent with previously reported compositions of lofted pyroCb aerosol plumes.[6,7,29,34] Analysis of particle mixing state revealed no major compositional differences between background survey flights and flights targeting convective influence, although survey flights shows slightly higher internal mixing and is consistent with previous observations.[15]

Collectively, these findings indicate that wildfire emissions are capable of episodically reshaping the stratospheric aerosol composition over North America, with potentially long-lasting but still uncertain effects. Since aerosols take months to deplete in the stratosphere, this transformation may be persistent or even irreversible as depleted BBOA material could be replaced by new injected material and enter steady-state concentration. Further work is needed to assess the implication of this change, including its effects on stratospheric aerosol radiative forcing, ozone chemistry, and the formation and persistence of polar stratospheric clouds.

Author contributions

S. S., Y. L., X. S., D. C., F. K., and A. L. devised the project and methodology. S. S., F. R. A., T. O., J. E., M. F., R. M., S. B., N. N. L., Z. C., S. C., M. A. M., and J. W. performed chemical imaging experiments and analyzed associated data. S. S., Y. L., X. S., and C. H. analyzed real-time data acquired during flights. S. S. and A. L. wrote the manuscript with contributions from all authors.

Conflicts of interest

There are no conflicts to declare.

Data availability

The data supporting this article has been included as part of the supplemental information (SI). Supplementary information: additional flight context, description of CCSEM/EDX measurements, spherical equivalent diameter calculations, and description of STXM/NEXAFS measurements. See DOI: **https://doi.org/10.1039/d5ea00127g**.

Acknowledgements

The DCOTSS mission and data analyses were supported by the National Aeronautics and Space Administration (NASA) grants 80NSSC19K1058, 80NSSC19K0326, and 80NSSC19K0347. We acknowledge partial support from the U.S. Department of Energy, Office of Biological and Environmental Research, Atmospheric System Research program (award DE-SC0021977) for measurements at Beamline 5.3.2.2 at the Advanced Light Source at Lawerence Berkeley National Laboratory and Beamline 10ID-1 at the Canadian Light Source. This research used resources of the Advanced Light Source, a U.S. DOE Office of Science User Facility under contract no. DE-AC02-05CH11231. This research used the CCSEM/EDX at the Environmental Molecular Sciences Laboratory which is DOE Office of Science User Facilities. EMSL is sponsored by the Biological and Environmental Research program and operated under Contract No. DE-AC05-76RL01830. Y. L. also acknowledges partial support from the NOAA Climate & Global Change Postdoctoral Fellowship Program (award NA23OAR4310383B).

References

1 D. M. Murphy, K. D. Froyd, J. P. Schwarz and J. C. Wilson, Observations of the chemical composition of stratospheric aerosol particles, *Q. J. R. Meteorol. Soc.*, 2014, **140**, 1269–1278.
2 C. E. Junge and J. E. Manson, Stratospheric aerosol studies, *J. Geophys. Res.*, 1961, **66**, 2163–2182.
3 C. E. Junge, C. W. Chagnon and J. E. Manson, Stratospheric Aerosols, *J. Meteor.*, 1961, **18**, 81–108.
4 D. M. Murphy, M. Abou-Ghanem, D. J. Cziczo, K. D. Froyd, J. Jacquot, M. J. Lawler, C. Maloney, J. M. C. Plane, M. N. Ross, G. P. Schill and X. Shen, Metals from spacecraft reentry in stratospheric aerosol particles, *Proc. Natl. Acad. Sci. U.S.A.*, 2023, **120**, e2313374120.
5 D. M. Murphy, D. S. Thomson and M. J. Mahoney, In Situ Measurements of Organics, Meteoritic Material, Mercury, and Other Elements in Aerosols at 5 to 19 Kilometers, *Science*, 1998, **282**, 1664–1669.
6 G. D'Angelo, S. Guimond, J. Reisner, D. A. Peterson and M. Dubey, Contrasting Stratospheric Smoke Mass and Lifetime From 2017 Canadian and 2019/2020 Australian Megafires: Global Simulations and Satellite Observations, *J. Geophys. Res.:Atmos.*, 2022, **127**, e2021JD036249.
7 K. Christian, J. Wang, C. Ge, D. Peterson, E. Hyer, J. Yorks and M. McGill, Radiative Forcing and Stratospheric Warming of Pyrocumulonimbus Smoke Aerosols: First Modeling Results With Multisensor (EPIC, CALIPSO, and CATS) Views from Space, *Geophys. Res. Lett.*, 2019, **46**, 10061–10071.
8 S. Das, P. R. Colarco, L. D. Oman, G. Taha and O. Torres, The long-term transport and radiative impacts of the 2017 British Columbia pyrocumulonimbus smoke aerosols in the stratosphere, *Atmos. Chem. Phys.*, 2021, **21**, 12069–12090.
9 O. Torres, P. K. Bhartia, G. Taha, H. Jethva, S. Das, P. Colarco, N. Krotkov, A. Omar and C. Ahn, Stratospheric Injection of Massive Smoke Plume From Canadian Boreal Fires in 2017 as Seen by DSCOVR-EPIC, CALIOP, and OMPS-LP Observations, *J. Geophys. Res.:Atmos.*, 2020, **125**, e2020JD032579.
10 P. Yu, D. M. Murphy, R. W. Portmann, O. B. Toon, K. D. Froyd, A. W. Rollins, R. Gao and K. H. Rosenlof, Radiative forcing from anthropogenic sulfur and organic emissions reaching the stratosphere, *Geophys. Res. Lett.*, 2016, **43**, 9361–9367.
11 S. Kremser, L. W. Thomason, M. Von Hobe, M. Hermann, T. Deshler, C. Timmreck, M. Toohey, A. Stenke, J. P. Schwarz, R. Weigel, S. Fueglistaler, F. J. Prata, J.-P. Vernier, H. Schlager, J. E. Barnes, J.-C. Antuña-Marrero, D. Fairlie, M. Palm, E. Mahieu, J. Notholt, M. Rex, C. Bingen, F. Vanhellemont, A. Bourassa, J. M. C. Plane, D. Klocke, S. A. Carn, L. Clarisse, T. Trickl, R. Neely, A. D. James, L. Rieger, J. C. Wilson and B. Meland, Stratospheric aerosol-

Observations, processes, and impact on climate: Stratospheric Aerosol, *Rev. Geophys.*, 2016, **54**, 278–335.

12 Y. Li, J. Dykema, T. Deshler and F. Keutsch, Composition Dependence of Stratospheric Aerosol Shortwave Radiative Forcing in Northern Midlatitudes, *Geophys. Res. Lett.*, 2021, **48**, e2021GL094427.

13 S. Khaykin, S. Bekki, S. Godin-Beekmann, M. D. Fromm, P. Goloub, Q. Hu, B. Josse, A. Laeng, M. Meziane, D. A. Peterson, S. Pelletier and V. Thouret, Stratospheric impact of the anomalous 2023 Canadian wildfires: the two vertical pathways of smoke, Aerosols/Remote Sensing/Stratosphere/Physics (physical properties and processes), *EGUsphere*, 2025, DOI: **10.5194/egusphere-2025-3152**.

14 W. J. Randel, M. Park, L. Emmons, D. Kinnison, P. Bernath, K. A. Walker, C. Boone and H. Pumphrey, Asian Monsoon Transport of Pollution to the Stratosphere, *Science*, 2010, **328**, 611–613.

15 X. Shen, J. L. Jacquot, Y. Li, S. A. L. Sharpe, J. A. Dykema, G. P. Schill, K. P. Bowman, C. R. Homeyer, M. Fraund, R. C. Moffet, T. E. Olayemi, J. V. Pittman, F. A. Rivera-Adorno, D. M. Murphy, J. B. Smith, A. Laskin, F. N. Keutsch and D. J. Cziczo, Stratospheric aerosol perturbation by tropospheric biomass burning and deep convection, *Nat. Geosci.*, 2025, DOI: **10.1038/s41561-025-01821-1**.

16 A. E. Dessler and S. C. Sherwood, Effect of convection on the summertime extratropical lower stratosphere, *J. Geophys. Res.*, 2004, **109**, 2004JD005209.

17 A. E. Gordon, C. R. Homeyer, J. B. Smith, R. Ueyama, J. M. Dean-Day, E. L. Atlas, K. Smith, J. V. Pittman, D. S. Sayres, D. M. Wilmouth, A. Pandey, J. M. St. Clair, T. F. Hanisco, J. Hare, R. A. Hannun, S. Wofsy, B. C. Daube and S. Donnelly, Airborne observations of upper troposphere and lower stratosphere composition change in active convection producing above-anvil cirrus plumes, *Atmos. Chem. Phys.*, 2024, **24**, 7591–7608.

18 Y. Hong, S. W. Nesbitt, R. J. Trapp and L. Di Girolamo, Near-global distributions of overshooting tops derived from Terra and Aqua MODIS observations, *Atmos. Meas. Tech.*, 2023, **16**, 1391–1406.

19 H. Jost, K. Drdla, A. Stohl, L. Pfister, M. Loewenstein, J. P. Lopez, P. K. Hudson, D. M. Murphy, D. J. Cziczo, M. Fromm, T. P. Bui, J. Dean-Day, C. Gerbig, M. J. Mahoney, E. C. Richard, N. Spichtinger, J. V. Pittman, E. M. Weinstock, J. C. Wilson and I. Xueref, In-situ observations of mid-latitude forest fire plumes deep in the stratosphere, *Geophys. Res. Lett.*, 2004, **31**, 2003GL019253.

20 J. M. Katich, E. C. Apel, I. Bourgeois, C. A. Brock, T. P. Bui, P. Campuzano-Jost, R. Commane, B. Daube, M. Dollner, M. Fromm, K. D. Froyd, A. J. Hills, R. S. Hornbrook, J. L. Jimenez, A. Kupc, K. D. Lamb, K. McKain, F. Moore, D. M. Murphy, B. A. Nault, J. Peischl, A. E. Perring, D. A. Peterson, E. A. Ray, K. H. Rosenlof, T. Ryerson, G. P. Schill, J. C. Schroder, B. Weinzierl, C. Thompson, C. J. Williamson, S. C. Wofsy, P. Yu and J. P. Schwarz, Pyrocumulonimbus affect average stratospheric aerosol composition, *Science*, 2023, **379**, 815–820.

21 Y. Li, J. Dykema, D. Peterson, X. Feng, X. Shen, N. June, M. Fromm, T. McHardy, J. Jacquot, J. Pittman, B. Daube, S. Wofsy, J. Dean-Day, A. Rapp, K. Bowman, D. Cziczo, L. Mickley, J. Pierce and F. Keutsch, Enhanced Radiative Cooling by Large Aerosol Particles from Pyrocumulonimbus, *Res Sq.*, 2024, DOI: **10.21203/rs.3.rs-5348977/v1**.

22 L. Pfister, R. Ueyama, E. J. Jensen and M. R. Schoeberl, Deep Convective Cloud Top Altitudes at High Temporal and Spatial Resolution, *Earth Space Sci.*, 2022, **9**, e2022EA002475.

23 J. W. Cooney, K. P. Bowman, C. R. Homeyer and T. M. Fenske, Ten Year Analysis of Tropopause-Overshooting Convection Using GridRad Data, *J. Geophys. Res.:Atmos.*, 2018, **123**, 329–343.

24 A. E. Waibel, H. Fischer, F. G. Wienhold, P. C. Siegmund, B. Lee, J. Ström, J. Lelieveld and P. J. Crutzen, Highly elevated carbon monoxide concentrations in the upper troposphere and lowermost stratosphere at northern midlatitudes during the STREAM II summer campaign in 1994, *Chemosphere:Global Change Sci.*, 1999, **1**, 233–248.

25 P. K. Hudson, D. M. Murphy, D. J. Cziczo, D. S. Thomson, J. A. De Gouw, C. Warneke, J. Holloway, H. Jost and G. Hübler, Biomass-burning particle measurements: Characteristic composition and chemical processing, *J. Geophys. Res.*, 2004, **109**, 2003JD004398.

26 A. E. Bourassa, L. A. Rieger, D. J. Zawada, S. Khaykin, L. W. Thomason and D. A. Degenstein, Satellite Limb Observations of Unprecedented Forest Fire Aerosol in the Stratosphere, *J. Geophys. Res.:Atmos.*, 2019, **124**, 9510–9519.

27 M. Burke, M. L. Childs, B. De La Cuesta, M. Qiu, J. Li, C. F. Gould, S. Heft-Neal and M. Wara, The contribution of wildfire to PM2.5 trends in the USA, *Nature*, 2023, **622**, 761–766.

28 M. Fromm, R. Servranckx, B. J. Stocks and D. A. Peterson, Understanding the critical elements of the pyrocumulonimbus storm sparked by high-intensity wildland fire, *Commun Earth Environ.*, 2022, **3**, 243.

29 K. Gorkowski, E. Koo, S. Jordan, J. Reisner, K. B. Benedict and M. Dubey, Insights into Pyrocumulus aerosol composition: black carbon content and organic vapor condensation, *Environ. Sci.: Atmos.*, 2024, **4**, 80–87.

30 P. Yu, O. B. Toon, C. G. Bardeen, Y. Zhu, K. H. Rosenlof, R. W. Portmann, T. D. Thornberry, R.-S. Gao, S. M. Davis, E. T. Wolf, J. De Gouw, D. A. Peterson, M. D. Fromm and A. Robock, Black carbon lofts wildfire smoke high into the stratosphere to form a persistent plume, *Science*, 2019, **365**, 587–590.

31 L. F. Radke, J. H. Lyons, P. V. Hobbs and R. E. Weiss, Smokes from the burning of aviation fuel and their self-lofting by solar heating, *J. Geophys. Res.*, 1990, **95**, 14071–14076.

32 D. A. Peterson, J. R. Campbell, E. J. Hyer, M. D. Fromm, G. P. Kablick, J. H. Cossuth and M. T. DeLand, Wildfire-driven thunderstorms cause a volcano-like stratospheric injection of smoke, *npj Clim Atmos Sci*, 2018, **1**, 30.

33 J. M. Reisner, A. J. Josephson, K. J. Gorkowski, E. Koo, D. K. Thompson, D. Schroeder and M. K. Dubey, Informed Multi-Scale Approach Applied to the British Columbia

Fires of Late Summer 2017, *J. Geophys. Res.:Atmos.*, 2023, **128**, e2022JD037238.

34 P. Beeler, J. Kumar, J. P. Schwarz, K. Adachi, L. Fierce, A. E. Perring, J. M. Katich and R. K. Chakrabarty, Light absorption enhancement of black carbon in a pyrocumulonimbus cloud, *Nat. Commun.*, 2024, **15**, 6243.

35 L. D. Yee, K. E. Kautzman, C. L. Loza, K. A. Schilling, M. M. Coggon, P. S. Chhabra, M. N. Chan, A. W. H. Chan, S. P. Hersey, J. D. Crounse, P. O. Wennberg, R. C. Flagan and J. H. Seinfeld, Secondary organic aerosol formation from biomass burning intermediates: phenol and methoxyphenols, *Atmos. Chem. Phys.*, 2013, **13**, 8019–8043.

36 K. P. Bowman, F. N. Keutsch, C. R. Homeyer, D. S. Sayres, J. B. Smith, D. M. Wilmouth, J. G. Anderson, E. L. Atlas, E. Apel, K. Bedka, T. P. Bui, D. Cziczo, B. Daube, E. R. Delaria, J. Dykema, T. F. Hanisco, R. Hannun, B. Hall, E. Hintsa, L. Howar, D. F. Hurst, J. L. Jacquot, A. Laskin, Y. Li, C. Liu, F. Moore, G. Mullendore, P. Newman, A. K. Pandit, A. D. Rapp, R. J. Salawitch, X. Shen, J. M. St. Clair, R. Ueyama, J.-P. Vernier and S. C. Wofsy, The Dynamics and Chemistry of the Summer Stratosphere (DCOTSS) Project, *Bull. Am. Meteorol. Soc.*, 2025, BAMSD2401771.

37 J. L. Jacquot, X. Shen, M. Abou-Ghanem, K. D. Froyd, M. Lawler, G. P. Schill, K. Slovacek, D. S. Thomson, D. J. Cziczo and D. M. Murphy, A new airborne single particle mass spectrometer: PALMS-NG, *Aerosol Sci. Technol.*, 2024, **58**, 991–1007.

38 Y. Li, C. Pedersen, J. Dykema, J.-P. Vernier, S. Vattioni, A. K. Pandit, A. Stenke, E. Asher, T. Thornberry, M. A. Todt, T. P. Bui, J. Dean-Day and F. N. Keutsch, In situ measurements of perturbations to stratospheric aerosol and modeled ozone and radiative impacts following the 2021 La Soufrière eruption, *Atmos. Chem. Phys.*, 2023, **23**, 15351–15364.

39 J. M. Tomlin, J. Weis, D. P. Veghte, S. China, M. Fraund, Q. He, N. Reicher, C. Li, K. A. Jankowski, F. A. Rivera-Adorno, A. C. Morales, Y. Rudich, R. C. Moffet, M. K. Gilles and A. Laskin, Chemical composition and morphological analysis of atmospheric particles from an intensive bonfire burning festival, *Environ. Sci.: Atmos.*, 2022, **2**, 616–633.

40 J. M. Tomlin, K. A. Jankowski, D. P. Veghte, S. China, P. Wang, M. Fraund, J. Weis, G. Zheng, Y. Wang, F. Rivera-Adorno, S. Raveh-Rubin, D. A. Knopf, J. Wang, M. K. Gilles, R. C. Moffet and A. Laskin, Impact of dry intrusion events on the composition and mixing state of particles during the winter Aerosol and Cloud Experiment in the Eastern North Atlantic (ACE-ENA), *Atmos. Chem. Phys.*, 2021, **21**, 18123–18146.

41 S. China, S. M. Burrows, B. Wang, T. H. Harder, J. Weis, M. Tanarhte, L. V. Rizzo, J. Brito, G. G. Cirino, P.-L. Ma, J. Cliff, P. Artaxo, M. K. Gilles and A. Laskin, Fungal spores as a source of sodium salt particles in the Amazon basin, *Nat. Commun.*, 2018, **9**, 4793.

42 M. Fraund, D. Pham, D. Bonanno, T. Harder, B. Wang, J. Brito, S. de Sá, S. Carbone, S. China, P. Artaxo, S. Martin, C. Pöhlker, M. Andreae, A. Laskin, M. Gilles and R. Moffet, Elemental Mixing State of Aerosol Particles Collected in Central Amazonia during GoAmazon2014/15, *Atmosphere*, 2017, **8**, 173.

43 M. Fraund, D. J. Bonanno, S. China, D. Q. Pham, D. Veghte, J. Weis, G. Kulkarni, K. Teske, M. K. Gilles, A. Laskin and R. C. Moffet, Optical properties and composition of viscous organic particles found in the Southern Great Plains, *Atmos. Chem. Phys.*, 2020, **20**, 11593–11606.

44 R. C. Moffet, R. E. O'Brien, P. A. Alpert, S. T. Kelly, D. Q. Pham, M. K. Gilles, D. A. Knopf and A. Laskin, Morphology and mixing of black carbon particles collected in central California during the CARES field study, *Atmos. Chem. Phys.*, 2016, **16**, 14515–14525.

45 F. A. Rivera-Adorno, J. M. Tomlin, N. N. Lata, L. Azzarello, M. A. Robinson, R. A. Washenfelder, A. Franchin, A. M. Middlebrook, S. China, S. S. Brown, C. J. Young, M. Fraund, R. C. Moffet and A. Laskin, Chemical Imaging of Atmospheric Biomass Burning Particles from North American Wildfires, *ACS EST Air*, 2025, **2**, 508–521.

46 A. Laskin, R. C. Moffet and M. K. Gilles, Chemical Imaging of Atmospheric Particles, *Acc. Chem. Res.*, 2019, **52**, 3419–3431.

47 NASA FIRMS, MODIS Standard Quality Thermal Anomalies/Fire Locations product MCD14ML distributed by NASA FIRMS, 2022-06-01, 2022-07–12.

48 C. R. Homeyer, J. B. Smith, K. M. Bedka, K. P. Bowman, D. M. Wilmouth, R. Ueyama, J. M. Dean-Day, J. M. St. Clair, R. Hannun, J. Hare, A. Pandey, D. S. Sayres, T. F. Hanisco, A. E. Gordon and E. N. Tinney, Extreme Altitudes of Stratospheric Hydration by Midlatitude Convection Observed During the DCOTSS Field Campaign, *Geophys. Res. Lett.*, 2023, **50**, e2023GL104914.

49 L. Giglio, J. Descloitres, C. O. Justice and Y. J. Kaufman, An Enhanced Contextual Fire Detection Algorithm for MODIS, *Remote Sens. Environ.*, 2003, **87**, 273–282.

50 H. Hersbach, B. Bell, P. Berrisford, S. Hirahara, A. Horányi, J. Muñoz-Sabater, J. Nicolas, C. Peubey, R. Radu, D. Schepers, A. Simmons, C. Soci, S. Abdalla, X. Abellan, G. Balsamo, P. Bechtold, G. Biavati, J. Bidlot, M. Bonavita, G. De Chiara, P. Dahlgren, D. Dee, M. Diamantakis, R. Dragani, J. Flemming, R. Forbes, M. Fuentes, A. Geer, L. Haimberger, S. Healy, R. J. Hogan, E. Hólm, M. Janisková, S. Keeley, P. Laloyaux, P. Lopez, C. Lupu, G. Radnoti, P. De Rosnay, I. Rozum, F. Vamborg, S. Villaume and J. Thépaut, The ERA5 global reanalysis, *Q. J. R. Meteorol. Soc.*, 2020, **146**, 1999–2049.

51 S. M. Griffin, K. M. Bedka and C. S. Velden, A Method for Calculating the Height of Overshooting Convective Cloud Tops Using Satellite-Based IR Imager and CloudSat Cloud Profiling Radar Observations, *Appl. Meteorol. Climatol.*, 2016, **55**, 479–491.

52 A. Laskin, R. C. Moffet, M. K. Gilles, J. D. Fast, R. A. Zaveri, B. Wang, P. Nigge and J. Shutthanandan, Tropospheric chemistry of internally mixed sea salt and organic particles: Surprising reactivity of NaCl with weak organic acids, *J. Geophys. Res.*, 2012, **117**, D15302.

53 A. Laskin, J. P. Cowin and M. J. Iedema, Analysis of individual environmental particles using modern methods

of electron microscopy and X-ray microanalysis, *J. Electron Spectrosc. Relat. Phenom.*, 2006, **150**, 260–274.

54 F. A. Rivera-Adorno, J. M. Tomlin, M. Fraund, E. Morgan, M. Laskin, R. Moffet and A. Laskin, Estimating viscosity of individual substrate-deposited particles from measurements of their height-to-width ratios, *Aerosol Sci. Technol.*, 2023, 1–10.

55 B. L. Henke, E. M. Gullikson and J. C. Davis, X-Ray Interactions: Photoabsorption, Scattering, Transmission, and Reflection at E = 50-30,000 eV, Z = 1-92, *At. Data Nucl. Data Tables*, 1993, **54**, 181–342.

56 R. C. Moffet, T. Henn, A. Laskin and M. K. Gilles, Automated Chemical Analysis of Internally Mixed Aerosol Particles Using X-ray Spectromicroscopy at the Carbon K-Edge, *Anal. Chem.*, 2010, **82**, 7906–7914.

57 R. C. Moffet, A. V. Tivanski and M. K. Gilles, Scanning X-ray Transmission Microscopy: Applications in Atmospheric Aerosol Research, in *Fundamentals and Applications in Aerosol Spectroscopy*, ed. R. Signorell and J. P. Reid, Taylor and Francis Books, Inc., 2010, pp. 419–462.

58 R. J. Hopkins, A. V. Tivanski, B. D. Marten and M. K. Gilles, Chemical bonding and structure of black carbon reference materials and individual carbonaceous atmospheric aerosols, *J. Aerosol Sci.*, 2007, **38**, 573–591.

59 M. Fraund, T. Park, L. Yao, D. Bonanno, D. Q. Pham and R. C. Moffet, Quantitative capabilities of STXM to measure spatially resolved organic volume fractions of mixed organic / inorganic particles, *Atmos. Meas. Tech.*, 2019, **12**, 1619–1633.

60 R. E. O'Brien, B. Wang, A. Laskin, N. Riemer, M. West, Q. Zhang, Y. Sun, X. Yu, P. Alpert, D. A. Knopf, M. K. Gilles and R. C. Moffet, Chemical imaging of ambient aerosol particles: Observational constraints on mixing state parameterization, *J. Geophys. Res. Atmos.*, 2015, **120**, 9591–9605.

61 J. L. Jimenez, M. R. Canagaratna, N. M. Donahue, A. S. H. Prevot, Q. Zhang, J. H. Kroll, P. F. DeCarlo, J. D. Allan, H. Coe, N. L. Ng, A. C. Aiken, K. S. Docherty, I. M. Ulbrich, A. P. Grieshop, A. L. Robinson, J. Duplissy, J. D. Smith, K. R. Wilson, V. A. Lanz, C. Hueglin, Y. L. Sun, J. Tian, A. Laaksonen, T. Raatikainen, J. Rautiainen, P. Vaattovaara, M. Ehn, M. Kulmala, J. M. Tomlinson, D. R. Collins, M. J. Cubison, E. J. Dunlea, J. A. Huffman, T. B. Onasch, M. R. Alfarra, P. I. Williams, K. Bower, Y. Kondo, J. Schneider, F. Drewnick, S. Borrmann, S. Weimer, K. Demerjian, D. Salcedo, L. Cottrell, R. Griffin, A. Takami, T. Miyoshi, S. Hatakeyama, A. Shimono, J. Y. Sun, Y. M. Zhang, K. Dzepina, J. R. Kimmel, D. Sueper, J. T. Jayne, S. C. Herndon, A. M. Trimborn, L. R. Williams, E. C. Wood, A. M. Middlebrook, C. E. Kolb, U. Baltensperger and D. R. Worsnop, Evolution of Organic Aerosols in the Atmosphere, *Science*, 2009, **326**, 1525–1529.

62 N. Riemer, A. P. Ault, M. West, R. L. Craig and J. H. Curtis, Aerosol Mixing State: Measurements, Modeling, and Impacts, *Rev. Geophys.*, 2019, **57**, 187–249.

63 K. Turhal, F. Plöger, J. Clemens, T. Birner, F. Weyland, P. Konopka and P. Hoor, Variability and trends in the potential vorticity (PV)-gradient dynamical tropopause, *Atmos. Chem. Phys.*, 2024, **24**, 13653–13679.

64 R. C. Moffet, T. C. Rödel, S. T. Kelly, X. Y. Yu, G. T. Carroll, J. Fast, R. A. Zaveri, A. Laskin and M. K. Gilles, Spectro-microscopic measurements of carbonaceous aerosol aging in Central California, *Atmos. Chem. Phys.*, 2013, **13**, 10445–10459.

65 K. Adachi and P. R. Buseck, Internally mixed soot, sulfates, and organic matter in aerosol particles from Mexico City, *Atmos. Chem. Phys.*, 2008, **8**, 6469–6481.

66 D. Pagonis, V. Selimovic, P. Campuzano-Jost, H. Guo, D. A. Day, M. K. Schueneman, B. A. Nault, M. M. Coggon, J. P. DiGangi, G. S. Diskin, E. C. Fortner, E. M. Gargulinski, G. I. Gkatzelis, J. W. Hair, S. C. Herndon, C. D. Holmes, J. M. Katich, J. B. Nowak, A. E. Perring, P. Saide, T. J. Shingler, A. J. Soja, L. H. Thapa, C. Warneke, E. B. Wiggins, A. Wisthaler, T. I. Yacovitch, R. J. Yokelson and J. L. Jimenez, Impact of Biomass Burning Organic Aerosol Volatility on Smoke Concentrations Downwind of Fires, *Environ. Sci. Technol.*, 2023, **57**, 17011–17021.

67 J. R. Holton, P. H. Haynes, M. E. McIntyre, A. R. Douglass, R. B. Rood and L. Pfister, Stratosphere-troposphere exchange, *Rev. Geophys.*, 1995, **33**, 403–439.

68 regionprops - Measure properties of image regions - MATLAB, **https://www.mathworks.com/help/images/ref/regionprops.html**, accessed 13 September 2025.

69 J. Zhang, Y. Wang, X. Teng, L. Liu, Y. Xu, L. Ren, Z. Shi, Y. Zhang, J. Jiang, D. Liu, M. Hu, L. Shao, J. Chen, S. T. Martin, X. Zhang and W. Li, Liquid-liquid phase separation reduces radiative absorption by aged black carbon aerosols, *Commun Earth Environ.*, 2022, **3**, 128.

70 W. Li, N. Riemer, L. Xu, Y. Wang, K. Adachi, Z. Shi, D. Zhang, Z. Zheng and A. Laskin, Microphysical properties of atmospheric soot and organic particles: measurements, modeling, and impacts, *npj Clim Atmos Sci*, 2024, **7**, 65.

71 T. C. Bond and R. W. Bergstrom, Light Absorption by Carbonaceous Particles: An Investigative Review, *Aerosol Sci. Technol.*, 2006, **40**, 27–67.

72 K. Adachi, S. H. Chung and P. R. Buseck, Shapes of soot aerosol particles and implications for their effects on climate, *J. Geophys. Res.*, 2010, **115**, 2009JD012868.

73 C. D. McClure, C. Y. Lim, D. H. Hagan, J. H. Kroll and C. D. Cappa, Biomass-burning-derived particles from a wide variety of fuels – Part 1: Properties of primary particles, *Atmos. Chem. Phys.*, 2020, **20**, 1531–1547.

74 N. Riemer and M. West, Quantifying aerosol mixing state with entropy and diversity measures, *Atmos. Chem. Phys.*, 2013, **13**, 11423–11439.

75 C. Shou, N. Riemer, T. B. Onasch, A. J. Sedlacek, A. T. Lambe, E. R. Lewis, P. Davidovits and M. West, Mixing state evolution of agglomerating particles in an aerosol chamber: Comparison of measurements and particle-resolved simulations, *Aerosol Sci. Technol.*, 2019, **53**, 1229–1243.